Generation of even and odd high harmonics in resonant metasurfaces using single and multiple ultra-intense laser pulses

Maxim Shcherbakov (✉ mrs356@cornell.edu)

  Cornell University

Haizhong Zhang

  Institute of Materials Research and Engineering, A*STAR (Agency for Science, Technology and Research)

Michael Tripepi

  Department of Physics, The Ohio State University   https://orcid.org/0000-0002-4657-9826

Giovanni Sartorello

  Cornell University

Noah Talisa

  Department of Physics, The Ohio State University

Abdallah AlShafey

  Department of Physics, The Ohio State University

Zhiyuan Fan

  Cornell University

Justin Twardowski

  Department of Physics, The Ohio State University

Leonid Krivitsky

  Institute of Materials Research and Engineering, A*STAR (Agency for Science, Technology and Research)

Arseniy Kuznetsov

  Institute of Materials Research and Engineering   https://orcid.org/0000-0002-7622-8939

Enam Chowdhury

  Department of Physics, The Ohio State University

Gennady Shvets

  Cornell University   https://orcid.org/0000-0001-8542-6753

Article

Generation of even and odd high harmonics in resonant metasurfaces using single and multiple ultra-intense laser pulses

Maxim R. Shcherbakov,[1,*] Haizhong Zhang,[2] Michael Tripepi,[3] Giovanni Sartorello,[1] Noah Talisa,[3] Abdallah AlShafey,[3] Zhiyuan Fan,[1] Justin Twardowski,[4] Leonid A. Krivitsky,[2] Arseniy I. Kuznetsov,[2] Enam Chowdhury,[3,4,5] Gennady Shvets[1,*]

Affiliations:

[1]School of Applied and Engineering Physics, Cornell University, Ithaca, NY 14853, USA.

[2]Institute of Materials Research and Engineering, A*STAR (Agency for Science, Technology and Research), 138634, Singapore.

[3]Department of Physics, The Ohio State University, Columbus, OH 43210, USA.

[4]Department of Material Science and Engineering, The Ohio State University, Columbus, OH 43210, USA.

[5]Department of Electrical and Computer Engineering, The Ohio State University, Columbus, OH 43210, USA.

*Correspondence to: mrs356@cornell.edu, gshvets@cornell.edu

High harmonic generation (HHG) opens a window on the fundamental science of strong-field light-mater interaction and serves as a key building block for attosecond optics and metrology. Resonantly enhanced HHG from hot spots in nanostructures is an attractive route to overcoming the well-known limitations of gases and bulk solids. We demonstrate a nanoscale platform for highly efficient HHG driven by strong mid-infrared laser pulses: an ultra-thin resonant gallium phosphide (GaP) metasurface. The wide bandgap and the lack of inversion symmetry of the GaP crystal enable the generation of even and odd harmonics covering a wide range of photon energies between 1.3 and 3 eV with minimal reabsorption. The resonantly enhanced conversion efficiency facilitates single-shot measurements that avoid material damage and pave the way to controllable transition between perturbative and non-perturbative regimes of light-matter interactions at the nanoscale.

Traditionally, high harmonics generation[1–4] has been observed in gases subjected to tunneling ionization by ultra-strong laser fields exceeding those that bind electrons to nuclei[5,6]. High ionization thresholds, inversion symmetry, and infrastructure requirements imposed by gas chambers present challenges to the development of small-footprint low-power sources integrable in existing optoelectronic platforms for efficient and broadband HHG. Solid-state materials represent an attractive alternative for tabletop HHG sources[7,8]. However, conventional approaches to HHG utilizing bulk crystals fail to simultaneously achieve high conversion efficiencies and broad spectral bandwidth owing to significant harmonics reabsorption and phase mismatch. More recently, designer nanostructures[9–14] have attracted considerable attention because they can potentially alleviate these problems due to locally enhanced optical "hot spot" fields through a variety of mechanisms: operation in the epsilon-near-zero regime, as in CdO,[14] high-quality-factor collective modes, which were demonstrated in Si metasurfaces[11], or

plasmonic field enhancement[9]. However, several challenges to achieving highly efficient HHG in the strong-field regime assisted by spectrally selective metasurfaces may be identified. First, narrow- and moderate-bandgap semiconductors, with bandgap energies Δ_g that are not much larger than the laser photon energy $\hbar\omega$, are damaged at moderate laser fluences due to multi-photon absorption followed by rapid free-carrier generation[15,16]. Moreover, the overabundance of free carriers can drastically reduce the quality (Q) factor of a resonant metasurface[17], thereby defeating its key purpose: the creation of resonantly-driven optical hot spots. Second, harmonics absorption by opaque materials reduces the HHG-emitting volume and dramatically decreases the HHG efficiency[18]. Finally, only a subset of harmonics (odd) can be produced by centrosymmetric materials. Currently, non-centrosymmetric materials enabling even-order harmonics[13,19] have not been utilized for nanostructure-based HHG: to date, high ($N \geq 4$) harmonics have only been reported from nanostructures biased by an external dc field[12] or 2D semiconductors[20].

Therefore, it is desirable to develop a photonic platform and an optical system providing both the access to non-perturbative physics (defined by a strong perturbation by a laser pulse of the electron/hole motion in their respective conduction/valence bands), as well as the ability to use HHG as a probe of the microscopic processes inside a crystal[20–23]. Such combination of a photonic platform and optical system must meet the following conditions: (a) the electronic bandgap of the constitutive material should be sufficiently large, so that multiple harmonic orders can be utilized; (b) the optical system should enable single-shot measurements that do not suffer from the inherent limitations of multi-pulse averaging, such as long-term damage[24–26] and measurement biases (e.g., produced by a single high-intensity outlier in a train of laser pulses); and (c) the photonic structure should enable the production of nanoscale regions of a strongly-

driven material phase embedded inside a weakly perturbed phase, thus opening the possibility of studying nonlocal effects in condensed matter phase without confounding laser damage.

The transition to nonlinear carrier motion occurs when the momentum gained from the laser electric field over a single period exceeds the size of the Brillouin zone of a solid material. This condition is expressed as $\beta \equiv \omega_B/2\omega > 1$,[8,21,27] where $\omega_B = eEa/\hbar$ is the Bloch oscillation frequency[28,29,30], a a crystalline period, ω is the laser frequency, $\hbar$ is the reduced Planck's constant, and E is the hot spot optical field. Concurrently, the injection of free carriers (FCs) into the conduction zone also takes place. The latter is governed by the dimensionless Keldysh parameter[31] $\gamma = \omega\sqrt{m^*\Delta_g}/eE$, where m^* is the effective electron mass. Approximately equal to the ratio of the carrier injection time to laser period, the Keldysh parameter characterizes electron tunneling across the bandgap. Therefore, highly-efficient non-perturbative (saturated) HHG requires that $\beta, \gamma^{-1} > 1$.

The key challenge addressed by our work is finding the appropriate photonic platofrm for entering this new regime without producing large numbers of FCs that can blue-shift[32] or dampen[17] the metasurface resonance. As illustrated by Figure S1 (see Supplementary Information Section 1 for the calculation of strong-field-induced FC generation), our choices of the metasurface material and laser wavelength $\lambda = 2\pi c/\omega$ are strongly constrained if we are to access the non-perturbative regime of HHG in nanostructures.

Here, we design and fabricate an ultrathin ($\approx \lambda/10$, where $\lambda = 3.95$ µm) photonic platform for enhanced HHG – a resonant metasurface – based on a transparent, high-index, wide-bandgap semiconductor: gallium phosphide (GaP)[33–35]. The combination of high refractive index ($n \approx 3$) and mid-infrared (MIR) transparency enables highly localized "hot spots" of the electromagnetic field inside GaP-based metasurfaces, akin to those made of silicon and gallium arsenide[36,37].

4

Large electronic band gap ($\Delta_g^{(dir)} = 2.78$ eV and $\Delta_g^{(indir)} = 2.24$ eV $\gg \hbar\omega$) of GaP drastically reduces multi-photon absorption of MIR light (see Supplementary Information Section 1) and prevents visible HHG reabsorption up to the $N = 7$ harmonic frequency $\omega_N \equiv N\omega$. Finally, the non-centrosymmetric zincblende crystal structure of GaP enables generation of even-order harmonics from the bulk[13,23].

This selection of the laser wavelength and the underlying metasurface material enabled us to produce record-breaking unsaturated conversion efficiencies into high harmonics even in the perturbative regime of moderate laser intensity $I_{max}^{(MP)} \approx 80$ GW/cm^2 in the multi-pulse (MP) illumination regime. By employing single-pulse (SP) measurements, we avoid laser-induced damage and reach the non-perturbative regime of HHG for incident laser intensities as high as $I_{max}^{(SP)} \approx 480$ GW/cm^2. We observe a resonance-dependent saturation of the HHG at high estimated values of normalized Bloch oscillation frequencies ($\beta \approx 2$), opening exciting new opportunities for non-perturbative light-matter interactions at the nanoscale.

The metasurfaces for enhanced HHG (Fig. 1a) were fabricated from 400 nm thick GaP films using thin film bonding, electron beam lithography and reactive ion etching (see Supplementary Information Section 2 for details). A scanning electron image of a typical metasurface sample is shown in Fig. 1b. The metasurfaces consist of densely packed domino-shaped dielectric resonant antennas (DRAs) supporting externally excited resonant electric dipole (ED) electromagnetic modes at the nominal resonant wavelength $\lambda_{res}^{(0)} = 3.95$ μm. These modes were experimentally identified for several metasurfaces with varying dimensions (and, correspondingly, varying resonant wavelengths $\lambda_{res} = \lambda_{res}^{(0)} + \delta\lambda_{res}$) using Fourier-transform infrared (FTIR) collimated beam spectroscopy[38]. At resonances – manifested as the transmission dips in the experimental

(Fig. 1d) and numerical (Fig. 1e) spectra due to the excitation of the ED modes of the DRAs –

metasurfaces funnel the MIR radiation into the "hot spots" (see Fig.1c for a numerical

simulation). The metasurface was nominally designed to provide moderate $\left|\frac{E_{loc}}{E_{ext}}\right|^2 \approx 10$ intensity

enhancement of the MIR radiation $\lambda = \lambda_{res}^{(0)}$. The most efficient excitation of an ED mode occurs

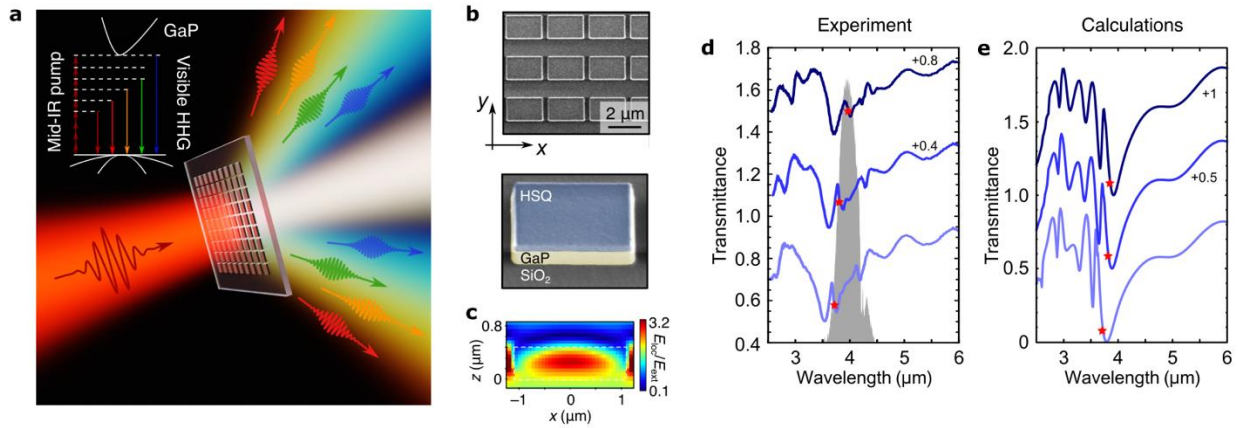when its spectral bandwidth matches that of the MIR pump shown in Fig. 1d in gray.

Figure 1. GaP metasurfaces for strong-field light-matter interactions in the mid-infrared | a. Illustration of the

HHG process: resonant GaP metasurfaces show efficient even and odd high harmonic generation (up to order H9)

due to the wide direct electronic bandgap, high refractive index and non-centrosymmetric lattice. The indirect band

gap is not shown. **b.** Fabricated GaP metasurfaces: SEM images. **c.** Calculated local field map of the metasurface

mode excited by a MIR pulse with $\lambda = \lambda_{res}^{(0)}$; peak local field enhancement: $|E_{loc}/E_{ext}|^2 \approx 10$ at resonant

wavelengths. **d.** Collimated (normal incidence) FTIR transmission spectra of three samples with varying DRA sizes:

largest (upper curve) to the smallest (lower curve) size. The second and third data sets are offset for clarity by +0.4

and +0.8, respectively. **e.** COMSOL simulations of **d**. The second and third data sets are offset for clarity by +0.5

and +1.0, respectively. Red stars indicate the estimated wavelengths of the maximum local field enhancement.

Figure 2a shows a simplified sketch of the experimental setup for the detection and

spectroscopy of HHG. Visible high harmonics are emitted from the metasurfaces driven by a

femtosecond ($\tau_{MIR} \approx 200$ fs) pulse train centered at a wavelength $\lambda = 3.95$ μm from a MIR

optical parametric oscillator. The harmonics detection was performed via back focal plane (BFP) imaging or with a visible spectrometer; see Supplementary Information Sections 3-5 for details. A typical HHG spectrum, with the luminescence background subtracted, is shown in Fig. 2b. Even- and odd-order harmonics are observed in the near-infrared and visible ranges: from $\hbar\omega_4 \approx$ 1.2 eV to $\hbar\omega_9 \approx$ 3.0 eV (where $\omega_N = 2\pi Nc/\lambda$ is the N'th harmonic frequency). No detectible harmonic signal was observed from either unstructured GaP film of the same thickness, or the SiO_2/Al_2O_3 substrate. The power of the 7th harmonic (H7) emitted from the sample was calibrated using an external laser source of the known power and a similar wavelength; see Supplementary Information Section 7 for the calibration procedure details. The absolute conversion efficiency reaches a value of $\eta_7 \sim 2 \cdot 10^{-9}$ for H7 at $I = 80$ GW/cm^2, i.e. two orders of magnitude larger than the previous demonstration in a metasurface[11] and more than one order of magnitude larger than that in an epsilon-near-zero material[14].
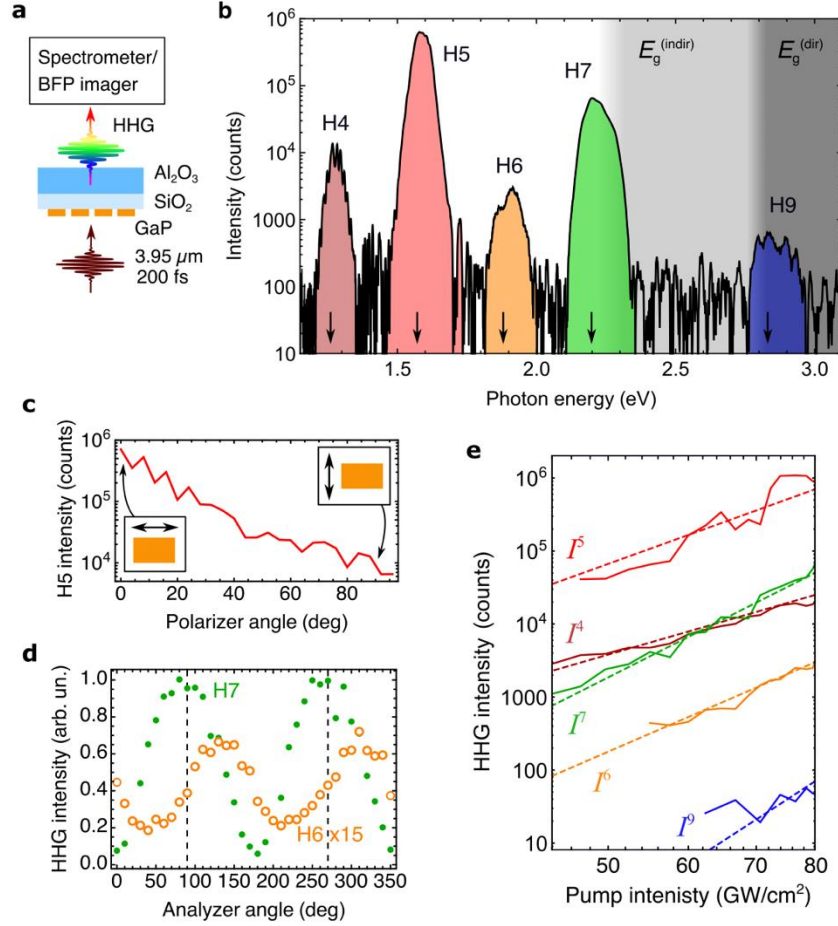
Figure 2. High harmonic generation in the perturbative multi-pulse (MP) regime | a. Simplified schematic of the HHG detection setup, with the detection arm represented by either a spectrometer or a back focal plane (BFP) imager. **b.** MP-HHG spectra of the resonant sample at $I_{MIR} = 80$ GW/cm^2. The $N = 8$ harmonic is not observed due to the onset of indirect interband transitions in GaP. The arrows indicate the predicted HHG wavelengths. **c.** Polarization dependence of H5 shows two orders of magnitude contrast between the resonant (horizontal) and non-resonant (vertical) MIR polarizations with $I_{MIR} = 100$ GW/cm^2. **d.** Linear polarization of the odd-order (H7: green dots) and elliptic polarization of the even-order (H6: orange circles) harmonics. Dashed lines: MIR laser pulse polarization ($I_{MIR} = 80$ GW/cm^2). **e.** Solid lines: HHG intensity as a function of the pump intensity for the $N = 4$ (dark-red), $N = 5$ (red), $N = 6$ (orange), $N = 7$ (green), and $N = 9$ (blue) orders. Dashed lines: corresponding guide-to-the-eye power laws, $I^{(N)} \sim I_{MIR}^N$.

Crucially, even-order (H4 and H6) harmonics were detected alongside the odd-order harmonics (H5, H7 and H9) because of the non-centrosymmetric (zinblende) crystal structure of GaP. Note that H8 was not detected in our experiment because of the combination of the indirect transitions at $\hbar\omega_8 = 2.28$ eV (making GaP partially opaque at H8) and the inherently lower conversion efficiency of the even-order harmonics. The relatively low efficiency of the even harmonics can be attributed to unfavorable orientation of the GaP principal crystalline axes inside the DRAs; it can be improved by about two orders of magnitude by a judicious choice of the crystal axis orientation (see Supplementary Information Section 8 and Supplementary Fig. S6).

To validate the importance of the dipole-active metasurfaces resonances, we have investigated the dependence of the H7 conversion efficiency on the polarization of the MIR pulse. The non-resonant pump polarization along the short side of the metasurface DRAs results in the efficiency reduction by two orders of magnitude compared with the resonant one as shown in Fig. 2c. This implies that optical field enhancement inside the hot spot produced by the resonant laser polarization aligned with the dipole moment of the ED mode is essential for the high efficiency of HHG observed in our experiments.

Next, we have analyzed the polarization states of the odd- and even-order harmonics. Specific examples for H7 and H6 harmonics are plotted in Fig. 2d for the (1, 0) diffraction order, as measured by BFP imaging. We observe that the odd harmonics (green dots) are co-polarized with the MIR pump (dashed lines). In contrast, the even harmonics (orange circles) are found to be elliptically polarized owing to the highly asymmetric structures of the even-order nonlinear susceptibility tensors $\chi_{ij...k}^{(N)}$,[39] where the Nth-order nonlinear polarization density of the medium is given by $P_i^{(N)} = \chi_{ij...k}^{(N)} E_j ... E_k$ (see Supplementary Information Section 8 for details). For odd

values of N, the diagonal matrix elements of $\chi_{ij\ldots k}^{(N)}$ dominate, and the Nth harmonic polarization

is collinear with that of the MIR pump. In contrast, for even N, the elements of the $\chi_{ij\ldots k}^{(N)}$ tensor

are predominantly off-diagonal, thereby enabling polarization changes of the even-order

harmonics.

To investigate whether the HHG in the multi-pulse (moderate peak power) regime obeys the

perturbative scaling laws, we have plotted in Fig. 2e the dependences of the harmonic intensity

$I^{(N)}$ on the MIR intensity I_{MIR}. The unsaturated dependences $I^{(N)} \sim I_{\mathrm{MIR}}^N$ are plotted as the guides

for the eye. In striking difference with the previous findings of HHG in nanostructures[11,14,40], the

response of the GaP metasurface does not exhibit any appreciable saturation. We conclude that

the perturbative regime of harmonics generation persists up to the maximum pump intensity

$(I_{\mathrm{MIR}} \approx I_{\max}^{(\mathrm{MP})} = 80 \ \mathrm{GW/cm^2})$ used in these experiments, which is equivalent to the hot spot

intensity $I_{\mathrm{hs}} \approx 0.7 \ \mathrm{TW/cm^2}$ inside the metasurface. This is in agreement with our estimates of

$\beta < 1$ for this range of intensities (see Table S1 of the SOM).

Because metasurfaces subjected to multi-pulse trains were visibly damaged for incident laser

intensities of order $I_{\mathrm{MIR}} \approx 200 \ \mathrm{GW/cm^2}$, the only non-destructive pathway to accessing the non-

perturbative regime of laser-matter interaction is to resort to single-pulse (SP) experiments.

Moreover, unlike MP averaging that may not provide the full picture of nonlinear processes, the

SP exposures yield accurate relationships between the pulse energy, HHG signal, and the

excitation site within the sample while avoiding the accumulation of MP damage[24–26]. In order to

access the high-intensity regime $(0.2 – 0.6 \ \mathrm{TW/cm^2})$, we replaced the focusing optics and

synchronized the elements of the setup. As schematically shown in Fig.3a, the OPA triggers a

mechanical shutter, which directs a single laser pulse to the sample and into the pick-off

detection arm. The sample resides on a three-dimensional translation stage and is monitored by a visible-light imaging system (not shown). Each area of the sample is exposed to a single laser pulse by moving it out of the laser path by 50 μm after each shot. For each shot, the trigger starts the fast camera acquisition that records BFP images of the HHG pattern; a typical single-shot BFP image is shown in Fig. 3b.
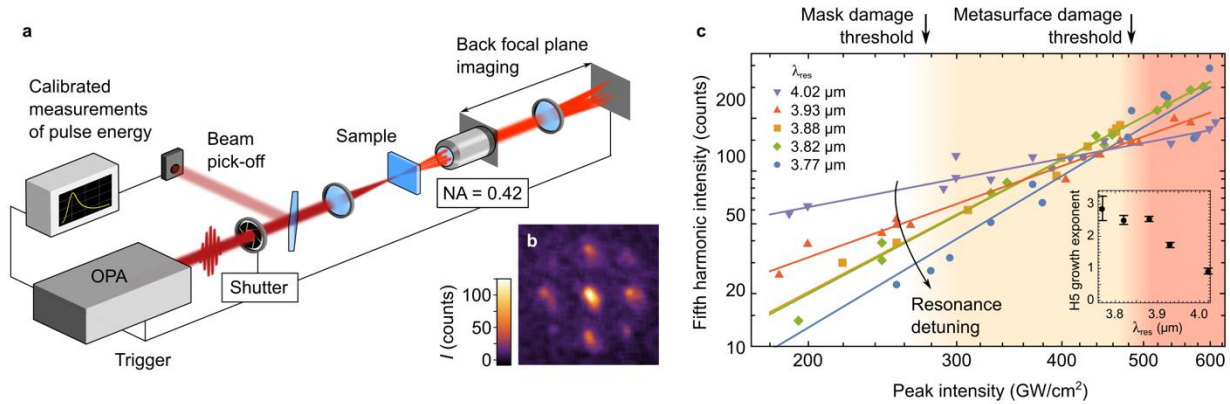

Figure 3. Single-pulse (SP) fifth harmonic generation reveals the non-perturbative regime and high damage thresholds of resonant metasurfaces | a. A setup for SP-HHG back focal plane (BFP) imaging. Single pulses pass through a mechanical shutter, split into the main beam (sample irradiation) and the pick-off beam (individual pulse power calibration). The diffracted harmonics are detected in the BFP configuration by triggered camera exposure. **b.** A typical BFP image of the H5 from the resonant sample at non-destructive intensities. **c.** Zeroth diffraction order intensity of the H5 as a function of MIR pump intensity for five different metasurfaces with resonances at λ_{res}, from the farthest from (blue circles) to the closest to (purple triangles) the driver wavelength. Solid lines: best fits to the power law $I^{(5)} = aI^b$. Deviation from the expected $I^{(5)} \sim I^5$ indicates the saturation of nonlinear response. Inset: power exponent b vs resonance wavelength λ_{res}. The mask damage threshold and the metasurface damage threshold are shown for the most resonant metasurface $\lambda_{res} = \lambda_{res}^{(0)} = \lambda$.

As an example, the zeroth diffraction order is plotted as a function of the field intensity in Fig. 3c for five different metasurfaces, from the one with the smallest detuning between the pump and the resonance (purple triangles: $\lambda_{res} = \lambda_{res}^{(0)}$) to the largest detuning (blue circles). The

solid lines show the best fits to the power law $I^{(5)} \sim aI^b$, where the exponent b is expected to be equal to 5 for the perturbative H5 process. However, in contrast with moderate-intensity data in Fig. 2e, the drastic reduction of the H5 exponent ($b < 5$) signifies the onset of the non-perturbative regime. The inset of Fig. 3c shows $b(\lambda_{res})$ as a function of the detuning between the incident pulse and the resonant wavelength λ_{res}. The exponent b varies monotonically between $b = 2.8$ for the least resonant metasurfaces to $b = 0.9$ for the most resonant metasurface.

The scanning electron micrographs (SEMs) of the degraded metasurfaces reveal two types of damage caused by the single pulses: the mask damage for $I_{MIR} > I_{max}^{(HSQ)} \approx 280 \text{ GW/cm}^2$ (detachments of the HSQ cap from the GaP resonators) and the structure damage for $I_{MIR} > I_{max}^{(GaP)} \approx 480 \text{ GW/cm}^2$ (removal of the GaP resonators from the substrate). Surprisingly, even though well-defined damage thresholds are identified by observing the metasurface degradation, no abrupt changes in HHG are experimentally observable at those threshold intensities $I_{max}^{(HSQ)}$ and $I_{max}^{(GaP)}$ (see Fig. 3c). The lack of any abrupt changes in the HHG dependences is attributed to the finite size of the beam: the HHG output is maintained at the beam's periphery even when the centrally positioned portion of the sample is damaged by a laser pulse. The estimated conversion efficiency of H5 in the single-pulse regime at $I = 200 \text{ GW/cm}^2$ for sample #5 (resonant case) is $\eta_{5\omega} = 1.4 \cdot 10^{-6}$, which is almost two orders of magnitude larger than that in the multi-pulse case. A comparison between various solid-state HHG sources, provided in Supplementary Table S2, shows that the GaP metasurface provides the largest specific (per unit length) conversion efficiency among all the materials provided.

One of the primary mechanisms contributing to the HHG in the non-perturbative regime is the generation of the nonlinear currents by the Bloch oscillations[29] of the FCs. The local (hot

spot) field strength that does not destroy the most resonant GaP metasurface (corresponding to $I_{MIR} \approx I_{max}^{(GaP)}$) can be estimated to be $E_{max}^{(hs)} \approx 0.24\ V/\text{Å}$ (assuming a factor $\times\ 10$ intensity enhancement at the hot spot), bringing the value of the Bloch frequency up to $\omega_B \approx 2 \cdot 10^{15}\ s^{-1}$. The corresponding ratio of the Bloch frequency to the driving MIR laser frequency is $\beta = \omega_B/2\omega \approx 2.1$, thus suggesting a transition to a non-perturbative response of the underlying GaP crystal (see Table S1). The anisotropic response of the electron subsystem suggests the importance of crystal lattice orientation, whereby one can tailor the contributions from different harmonics by engineering the crystal axes with respect to the nanostructure. These effects comprise an intriguing topic for future studies.

In conclusion, we have demonstrated efficient visible high harmonics generation using mid-infrared resonances in ultra-thin gallium phosphide metasurfaces. Our approach provides record-high conversion efficiency at the nanoscale, enabled by the combination of strong hot spot enhancement of the optical field, high resilience of the underlying material to strong fields, and the low level of HHG reabsorption. Single-pulse illumination format enabled us to utilize much higher laser intensities than in the multiple-pulse format, thereby accessing the non-perturbative regime of HHG without confounding structural damage. The robustness of the metasurface to laser damage under ultra-intense illumination opens new routes to accessing strong-field regimes with tailored light fields and enables non-perturbative light-matter interactions on a chip.

References and Notes:

1.   Paul, P. M. *et al.* Observation of a train of attosecond pulses from high harmonic generation. *Science (80-.).* **292**, 1689–1692 (2001).

2.   Krausz, F. & Ivanov, M. Attosecond physics. *Rev. Mod. Phys.* **81**, 163–234 (2009).

3.   McPherson, A. *et al.* Studies of multiphoton production of vacuum-ultraviolet radiation in the rare gases. *J. Opt. Soc. Am. B* **4**, 595 (1987).

4.   Ferray, M. *et al.* Multiple-harmonic conversion of 1064 nm radiation in rare gases. *J. Phys. B At. Mol. Opt. Phys.* **21**, (1988).

5.   Schafer, K. J., Yang, B., Dimauro, L. F. & Kulander, K. C. Above threshold ionization beyond the high harmonic cutoff. *Phys. Rev. Lett.* **70**, 1599–1602 (1993).

6.   Bartels, R. *et al.* Shaped-pulse optimization of coherent emission of high-harmonic soft x-rays. *Nature* **406**, 164–166 (2000).

7.   Ghimire, S. *et al.* Observation of high-order harmonic generation in a bulk crystal. *Nat. Phys.* **7**, 138–141 (2011).

8.   Ghimire, S. & Reis, D. A. High-harmonic generation from solids. *Nat. Phys.* **15**, 10–16 (2019).

9.   Vampa, G. *et al.* Plasmon-enhanced high-harmonic generation from silicon. *Nat. Phys.* **13**, 659–662 (2017).

10.   Sivis, M. *et al.* Tailored semiconductors for high-harmonic optoelectronics. *Science (80-.).* **306**, 303–306 (2017).

11.   Liu, H. *et al.* Enhanced high-harmonic generation from an all-dielectric metasurface. *Nat. Phys.* **14**, 1006–1010 (2018).

12.   Vampa, G. *et al.* Strong-field optoelectronics in solids. *Nat. Photonics* **12**, 465–468 (2018).

13. Liu, S. *et al.* An all-dielectric metasurface as a broadband optical frequency mixer. *Nat. Commun.* **9**, 2507 (2018).

14. Yang, Y. *et al.* High-harmonic generation from an epsilon-near-zero material. *Nat. Phys.* **15**, 1022–1026 (2019).

15. Austin, D. R. *et al.* Femtosecond laser damage of germanium from near- to mid-IR wavelengths. *Opt. Lett.* **43**, 3702–3705 (2018).

16. Werner, K. *et al.* Single-Shot Multi-Stage Damage and Ablation of Silicon by Femtosecond Mid-infrared Laser Pulses. *Sci. Rep.* **9**, 1–13 (2019).

17. Shcherbakov, M. R. *et al.* Time-variant metasurfaces enable tunable spectral bands of negative extinction. *Optica* **6**, 1441 (2019).

18. Liu, H. *et al.* Overcoming the absorption limit in high-harmonic generation from crystals. (2019).

19. Liu, S. *et al.* Resonantly Enhanced Second-Harmonic Generation Using III--V Semiconductor All-Dielectric Metasurfaces. *Nano Lett.* **16**, 5426–5432 (2016).

20. Liu, H. *et al.* High-harmonic generation from an atomically thin semiconductor. *Nat. Phys.* **13**, 262–265 (2016).

21. Vampa, G. *et al.* Theoretical analysis of high-harmonic generation in solids. *Phys. Rev. Lett.* **113**, 073901 (2014).

22. Hafez, H. A. *et al.* Extremely efficient terahertz high-harmonic generation in graphene by hot Dirac fermions. *Nature* **561**, 507–511 (2018).

23. Hohenleutner, M. *et al.* Real-time observation of interfering crystal electrons in high-

harmonic generation. *Nature* **523**, 572–575 (2015).

24. Leitner, T. *et al.* Shot-to-shot and average absolute photon flux measurements of a femtosecond laser high-order harmonic photon source. *New J. Phys.* **13**, 093003 (2011).

25. Goh, S. J. *et al.* Single-shot fluctuations in waveguided high-harmonic generation. *Opt. Express* **23**, 24888 (2015).

26. Nisoli, M. *et al.* Effects of carrier-envelope phase differences of few-optical-cycle light pulses in single-shot high-order-harmonic spectra. *Phys. Rev. Lett.* **91**, 213905 (2003).

27. Ghimire, S. *et al.* Observation of high-order harmonic generation in a bulk crystal. *Nat. Phys.* **7**, 138–141 (2011).

28. Ghimire, S. *et al.* Strong-field and attosecond physics in solids. *J. Phys. B At. Mol. Opt. Phys.* **47**, 204030 (2014).

29. Schubert, O. *et al.* Sub-cycle control of terahertz high-harmonic generation by dynamical Bloch oscillations. *Nat. Photonics* **8**, 119–123 (2014).

30. Wu, M., Ghimire, S., Reis, D. A., Schafer, K. J. & Gaarde, M. B. High-harmonic generation from Bloch electrons in solids. *Phys. Rev. A* **91**, 043839 (2015).

31. Keldysh, L. V. Ionization in the Field of a Strong Electromagnetic Wave. *J. Exptl. Theor. Phys.* **20**, 1307–1314 (1965).

32. Shcherbakov, M. R. *et al.* Photon acceleration and tunable broadband harmonics generation in nonlinear time-dependent metasurfaces. *Nat. Commun.* **10**, 1345 (2019).

33. Rivoire, K., Lin, Z., Hatami, F., Ted Masselink, W. & Vučković, J. Second harmonic generation in gallium phosphide photonic crystal nanocavities with ultralow CW pump

power. *Opt. Express* **17**, 22609–22615 (2009).

34.   Logan, A. D. *et al.* 400%/W second harmonic conversion efficiency in 14 μm-diameter

        gallium phosphide-on-oxide resonators. *Opt. Express* **26**, 33687 (2018).

35.   Wilson, D. J. *et al.* Integrated gallium phosphide nonlinear photonics. *Nat. Photonics* **14**,

        57–62 (2020).

36.   Kuznetsov, A. I., Miroshnichenko, A. E., Brongersma, M. L., Kivshar, Y. S. &

        Lukyanchuk, B. Optically resonant dielectric nanostructures. *Science (80-.).* **354**, aag2472

        (2016).

37.   Koshelev, K. *et al.* Subwavelength dielectric resonators for nonlinear nanophotonics.

        Science (80-.). **367**, 288–292 (2020).

38.   Wu, C. *et al.* Spectrally selective chiral silicon metasurfaces based on infrared Fano

        resonances. *Nat. Commun.* **5**, 3892 (2014).

39.   Boyd, R. *Nonlinear Optics*. (Elsevier, 2008).

40.   Yoshikawa, N., Tamaya, T. & Tanaka, K. High-harmonic generation in graphene

        enhanced by elliptically polarized light excitation. *Science (80-.).* **356**, 736–738 (2017).

Methods

For the list and description of methods, see Supplementary information.

Author Contributions

M. R. S., G. Shvets and A. I. K. conceived the idea. M. R. S. and Z. F. designed the sample. H. Z., L. A. K. and A. I. K. fabricated the samples. G. Sartorello measured the infrared transmittance spectra of the samples. M. R. S., M. T., G. Sartorello, N. T., A. A., J. T. and E. C. performed the nonlinear optical measurements. M. R. S. prepared the initial draft of the manuscript. A. I. K., E. C. and G. Shvets supervised the project. All authors contributed to the final version of the manuscript.

Competing interests

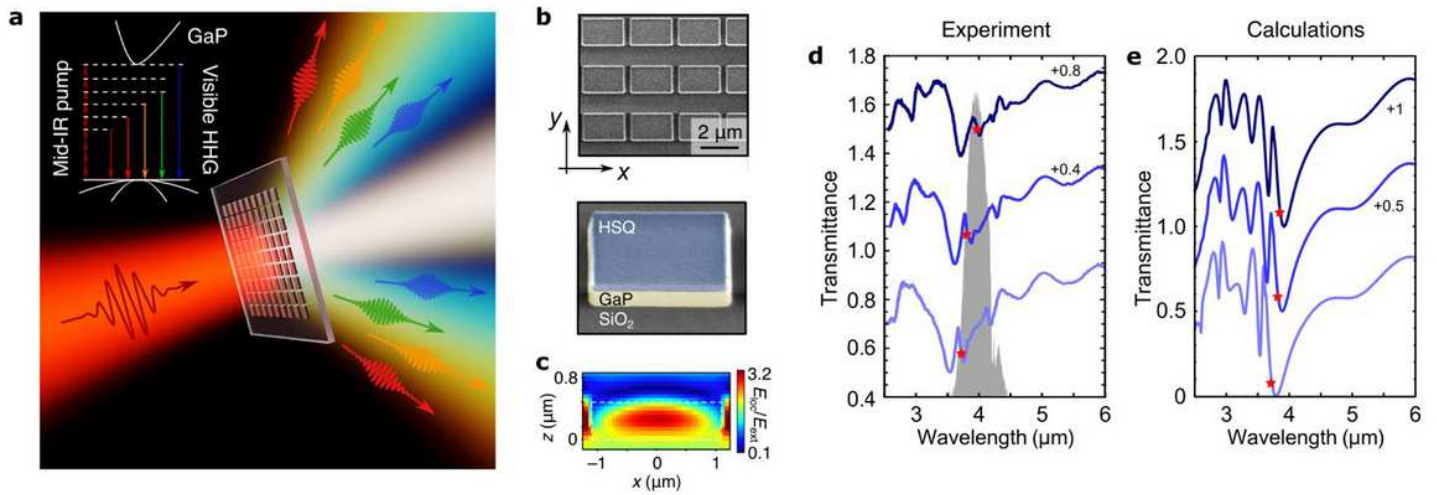The authors declare no competing interests.

Figures

Figure 1

GaP metasurfaces for strong-field light-matter interactions in the mid-infrared | a. Illustration of the HHG process: resonant GaP metasurfaces show efficient even and odd high harmonic generation (up to order H9) due to the wide direct electronic bandgap, high refractive index and non-centrosymmetric lattice. The indirect band gap is not shown. b. Fabricated GaP metasurfaces: SEM images. c. Calculated local field map of the metasurface mode excited by a MIR pulse with $\omega = \omega_{res}(0)$; peak local field enhancement: $|E_{loc}/E_{ext}|^2 \approx 10$ at resonant wavelengths. d. Collimated (normal incidence) FTIR transmission spectra of three samples with varying DRA sizes: largest (upper curve) to the smallest (lower curve) size. The second and third data sets are offset for clarity by +0.4 and +0.8, respectively. e. COMSOL simulations of d. The second and third data sets are offset for clarity by +0.5 and +1.0, respectively. Red stars indicate the estimated wavelengths of the maximum local field enhancement.
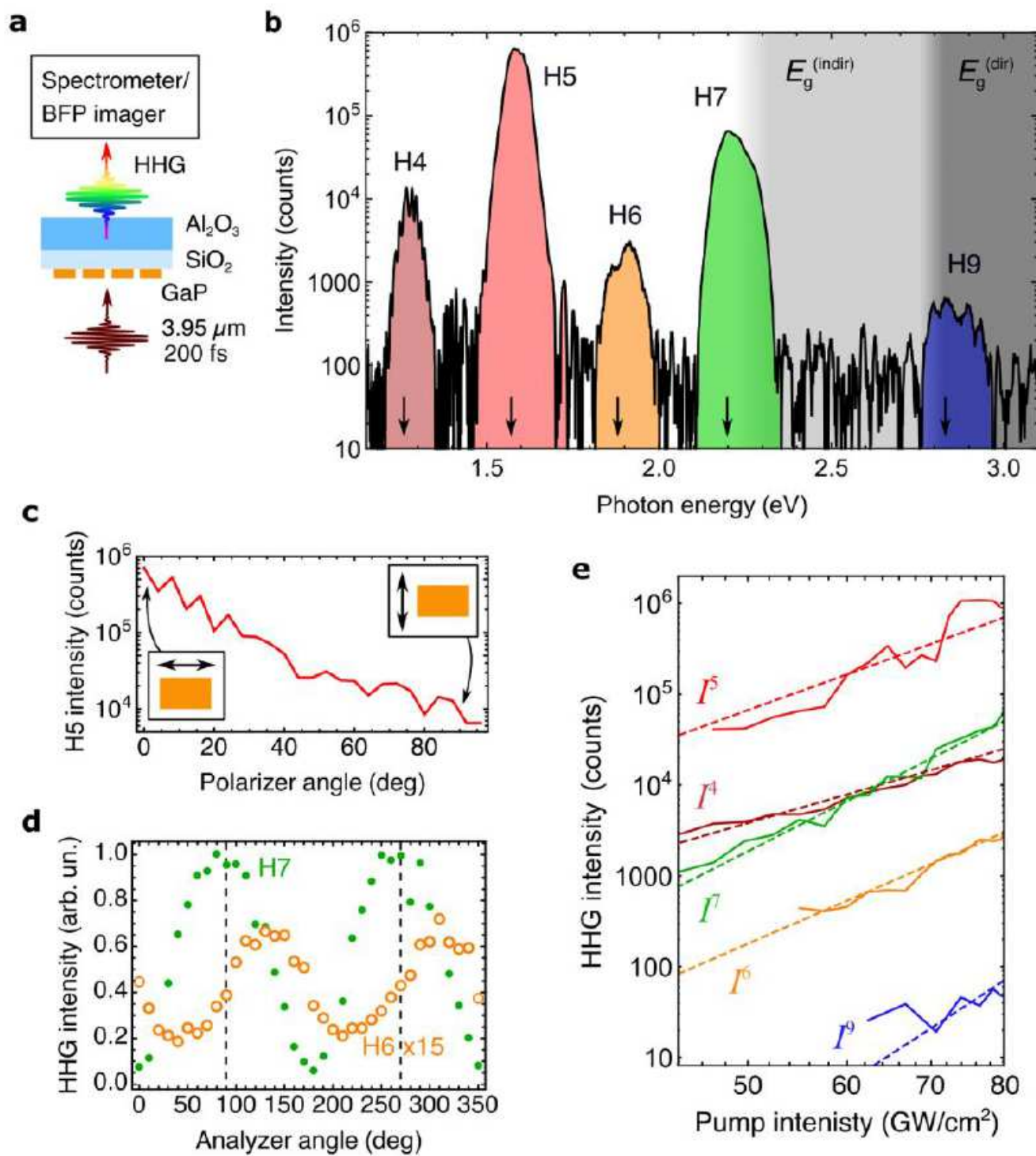
Figure 2

High harmonic generation in the perturbative multi-pulse (MP) regime | a. Simplified schematic of the HHG detection setup, with the detection arm represented by either a spectrometer or a back focal plane (BFP) imager. b. MP-HHG spectra of the resonant sample at I_{MIR}=80 GW/cm2. The N = 8 harmonic is not observed due to the onset of indirect interband transitions in GaP. The arrows indicate the predicted HHG wavelengths. c. Polarization dependence of H5 shows two orders of magnitude contrast between the

resonant (horizontal) and non-resonant (vertical) MIR polarizations with I_{MIR}=100 GW/cm2. d. Linear polarization of the odd-order (H7: green dots) and elliptic polarization of the even-order (H6: orange circles) harmonics. Dashed lines: MIR laser pulse polarization (I_{MIR}=80 GW/cm2). e. Solid lines: HHG intensity as a function of the pump intensity for the N = 4 (dark-red), N = 5 (red), N = 6 (orange), N = 7 (green), and N = 9 (blue) orders. Dashed lines: corresponding guide-to-the-eye power laws, $I(N) \sim I_{MIR}^N$.
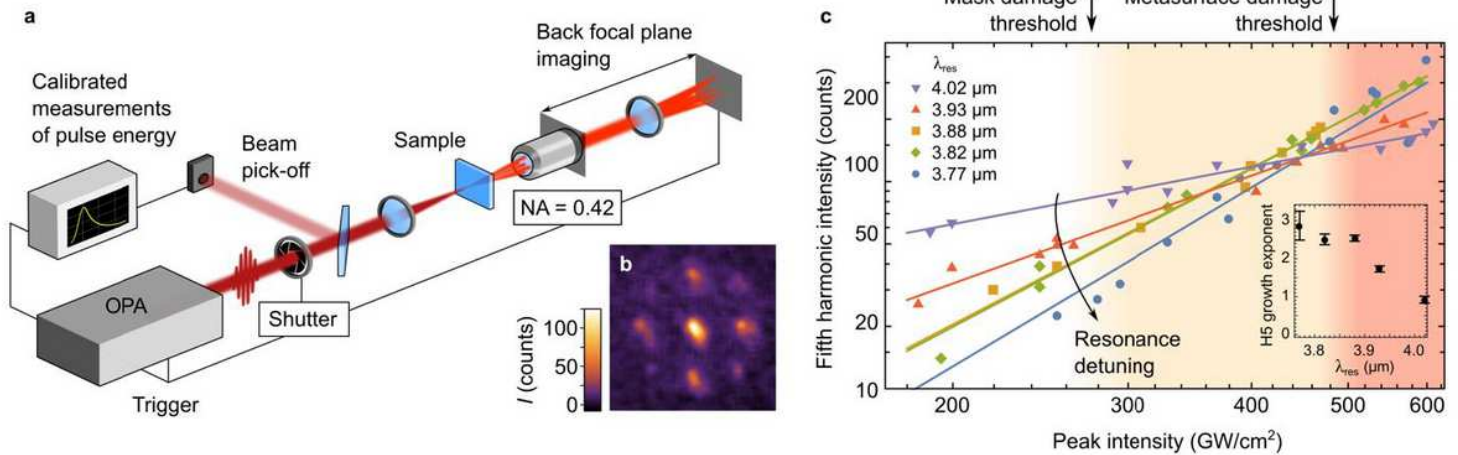

Figure 3

Single-pulse (SP) fifth harmonic generation reveals the non-perturbative regime and high damage thresholds of resonant metasurfaces | a. A setup for SP-HHG back focal plane (BFP) imaging. Single pulses pass through a mechanical shutter, split into the main beam (sample irradiation) and the pick-off beam (individual pulse power calibration). The diffracted harmonics are detected in the BFP configuration by triggered camera exposure. b. A typical BFP image of the H5 from the resonant sample at non-destructive intensities. c. Zeroth diffraction order intensity of the H5 as a function of MIR pump intensity for five different metasurfaces with resonances at λ_{res}, from the farthest from (blue circles) to the closest to (purple triangles) the driver wavelength. Solid lines: best fits to the power law $I(5) = I^\gamma$. Deviation from the expected $I(5) \sim I^5$ indicates the saturation of nonlinear response. Inset: power exponent γ vs resonance wavelength λres. The mask damage threshold and the metasurface damage threshold are shown for the most resonant metasurface $\lambda_{res}=\lambda_{res}(0)=\lambda$.

Supplementary Files

This is a list of supplementary files associated with this preprint. Click to download.

- ShcherbakovSOM.pdf
- supplementarynotebook.txt